

X-Ray Transitions from Antiprotonic Noble Gases

D. Gotta^{1a}, K. Rashid^{2b}, B. Fricke³, P. Indelicato⁴, and L. M. Simons^{5c}

¹ Institut für Kernphysik, Forschungszentrum Jülich, D-52425 Jülich, Germany

² Department of Computer Science, Bahria University, Sector E-8, Islamabad 44000, Pakistan

³ Institut für Physik, Universität Kassel, D-34132 Kassel, Germany

⁴ Laboratoire Kastler Brossel, UPMC-Paris 6 ENS CNRS; Case 74, 4 place Jussieu, F-75005 Paris, France

⁵ Laboratory for Particle Physics, Paul Scherrer Institut, CH-5232 Villigen, Switzerland

Received: date / Revised version: date

Abstract. The onset of antiprotonic X-ray transitions at high principal quantum numbers and the occurrence of electronic X-rays in antiprotonic argon, krypton, and xenon has been analyzed with the help of Multiconfiguration Dirac-Fock calculations. The shell-by-shell ionisation by Auger electron emission, characterised by appearance and disappearance of X-ray lines, is followed through the antiprotonic cascade by considering transition and binding energies of both the antiproton and the remaining electrons. Electronic lines could be attributed partly to specific states of the antiprotonic atom de-excitation.

PACS. 36.10.-k Exotic atoms – 32.30.Rj X-ray spectra

1 Introduction

The capture of an antiproton by atoms into a Coulombic bound orbit and the first stages of its subsequent de-excitation in the presence of the remaining electron cloud is a highly complicated many-body process. Experimental investigations of the upper cascade are difficult because of the small energy gain in the initial steps as is the theoretical description because of the interplay of competing processes.

Capture occurs when the antiproton is slowed down to a few tens eV of kinetic energy, where collisions, electron excitation and ejection open channels for an antiprotonic transition from the continuum into a highly excited quantum state of the Coulomb potential of the nucleus. At the beginning of de-excitation the antiproton experiences a significantly screened Coulomb force due to the many remaining electrons. Cascading through the electron cloud the antiproton knocks out more electrons and rapidly approaches the nucleus. After reaching lower-lying levels de-excitation takes place predominantly by X-ray emission. Finally the overlap of the orbitals with the nucleus leads to annihilation (Fig. 1). Details on capture and atomic cascade may be found in [1, 2, 3, 4, 5, 6, 7, 8].

As a rule of thumb the quantum cascade of the captured antiproton starts at large principal quantum numbers at about distances of the outermost electron shell.

^a corresponding author: d.gotta@fz-juelich.de

^b present address: National Centre for Physics, QAU campus, Islamabad 44000, Pakistan

^c present address: Departamento de Física da Universidade de Coimbra, 3004-516 Coimbra, Portugal

This corresponds to $n_p^{initial} = n_e \sqrt{m_p/m_e}$, where n_e is the principal quantum number of this electron shell. A first Auger emission at capture may be followed by additional electron removal due to shake-off being nearly equally important for all nuclear charges [9]. Calculations suggest that radiative capture is negligible [1], which has been confirmed experimentally in the case of muonic atoms [10, 11]. Hence, the measurement of X-rays originating from early

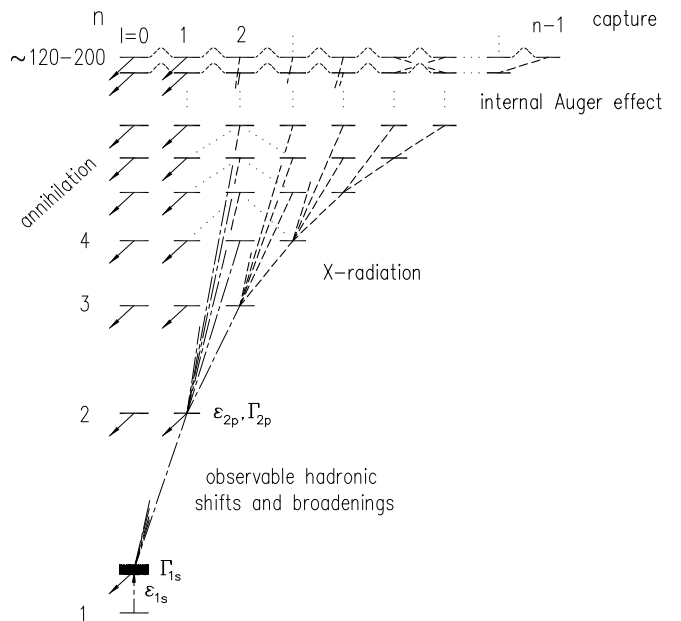


Fig. 1. De-excitation cascade in a light antiprotonic atom.

steps of the electromagnetic cascade provides a way to obtain detailed information on the dynamics of the depletion of the electron shells. For antiprotonic argon, krypton, and xenon with $n_e = 3, 4$, and 5 for the outermost electron shells, $n_{\bar{p}} = 128, 170$, and 215 allowing a much larger number of de-excitation steps than in muonic or pionic atoms.

Cascade models assume at capture a modified statistical distribution of the angular momentum states ℓ according to $P(n, \ell) \propto (2\ell + 1)e^{\alpha\ell}$, where α is a phenomenological parameter obtained from adjusting X-ray intensities to the measured line yields [12]. The value of $\alpha = 0$ corresponds to a purely statistical distribution. Usually muonic and pionic data are described better by modified statistical distributions typically with the modulus of α being less than 0.2 , but varying from element to element and even with the target chemistry [7, 11, 13, 14, 15, 16]. However, it must be emphasized that the population at capture is derived from X-ray transitions between low-lying states, i.e., it is more or less a reasonable starting point for cascade calculations but – in particular in the case of antiprotons – far below the initial capture states. Theoretical studies suggest that the initial quantum number $n_{\bar{p}}$ is expected to show a broad distribution but peaked at about $n_{\bar{p}}^{\text{initial}}$ and with different ℓ distributions for each $n_{\bar{p}}$ [17].

For medium and high Z atoms the cascade time from formation to annihilation is of the order of picoseconds or less, especially because of the very fast Auger process [18, 19]. Therefore, during the antiproton's descent, electrons are continuously removed leading to a depletion of electron shells. Significant Auger electron emission has been found in kaonic and muonic atom experiments [20, 21].

In dilute gases, electron refilling from neighbouring atoms or molecules is strongly suppressed during the short cascade time. Consequently, for light and medium- Z atoms the number of Auger transitions is sufficient for complete ionisation of the L and higher shells. This was established by the observation of X-ray transitions saturated in intensity for elements up to krypton along with a reduction of the X-ray yield when the K-electron emission threshold is reached at $n_{\bar{p}} \approx 16$ (Fig. 2). Absolute line yields of the order of 90% are observed [22, 23] and a distinction of the transition energy for antiprotonic atoms with and without K-shell electrons becomes necessary (Table 1).

The frequent Auger emission of electrons during the antiproton's descent causes a continuous and successive rearrangement of the electron configurations. Because electrons are much less massive than the antiproton their de-excitation occurs immediately whereas atomic antiprotonic states are comparatively long-living. While radiative vacancy de-excitation is significant for K holes for krypton and higher Z , non-radiative de-excitation dominates for L shells up to $Z \approx 90$ [24]. Therefore, the appearance of electronic L-X-rays yields information on the ionisation state.

The de-excitation of an exotic-atom cascade does not lead to an excessive vacancy cascade in contrast to normal atoms [25]. It occurs stepwise, because K- or L-shell Auger

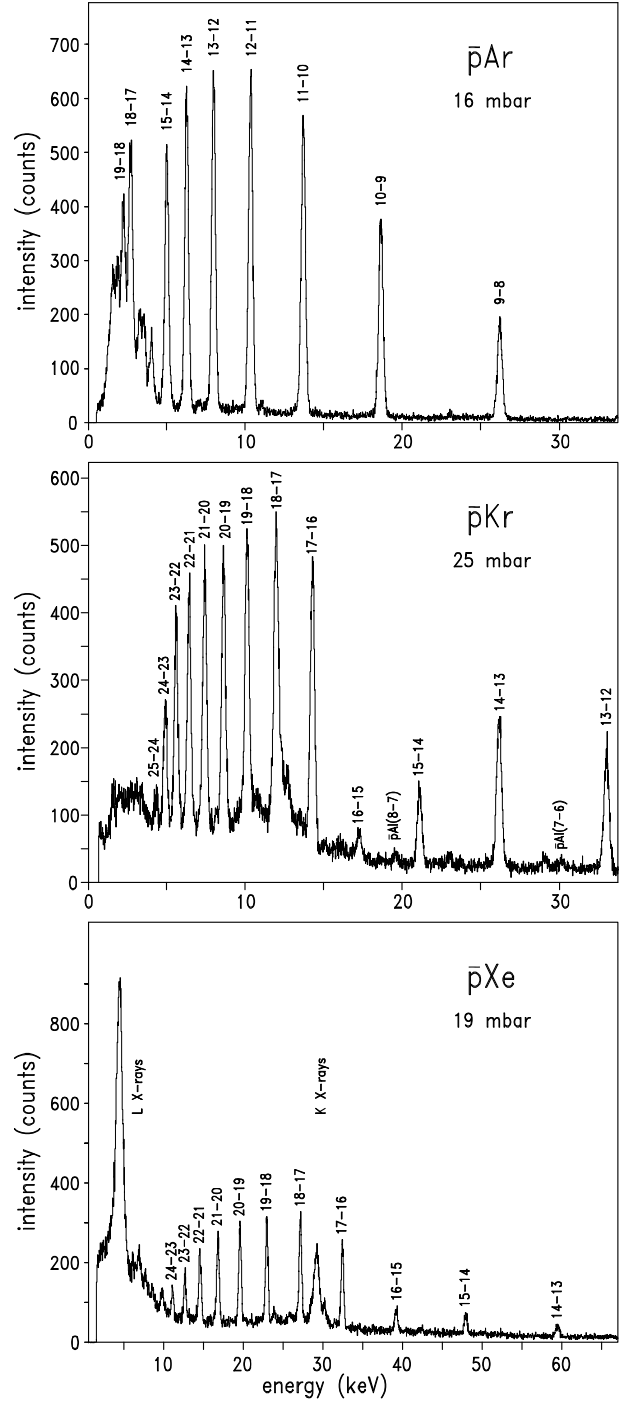


Fig. 2. X-ray spectra of antiprotonic argon, krypton, and xenon.

emission can take place only after the antiproton reaches a sufficiently deep bound state. By then, the outer shells are already strongly depleted (see Sec. 3).

In the spectra of antiprotonic argon, krypton, and xenon, additional lines appear having about the same energies as electronic K and L lines and are in the range of antiprotonic transitions with $n_{\bar{p}} = 18 \rightarrow 17$ and $n_{\bar{p}} = 17 \rightarrow 16$ and around $n_{\bar{p}} = 30$, respectively (Fig. 2). The intensity of these lines increases with nuclear charge, i.e., with the

Table 1. Transition energies between circular states in antiprotonic atoms argon, krypton, and xenon atoms, which are electron-free and with 2 remaining K electrons. The first two antiprotonic $\Delta n_{\bar{p}} = 1$ transitions, which are able to ionise the K-shell electrons are printed bold face.

Z	18	18	36	36	54	54
$n_{\bar{p}}$	$\bar{p}\text{Ar}$	$\bar{p}\text{Ar}2e^-$	$\bar{p}\text{Kr}$	$\bar{p}\text{Kr}2e^-$	$\bar{p}\text{Xe}$	$\bar{p}\text{Xe}2e^-$
\rightarrow						
$n_{\bar{p}} - 1$	energy (eV)					
8-7	37193					
9-8	25972					
10-9	18566					
11-10	13729					
12-11	10438					
13-12	8120		32965			
14-13	6441		26145		59167	
15-14	5196		21084		47708	
16-15	4251	4249	17250		39028	39018
17-16	3523	3520	14292	14286	32333	32321
18-17	2952	2949	11974	11967	27086	27073
19-18	2498	2495	10130	10123	22916	22901
20-19	2133	2129	8649	8639	19560	19543
21-20	1835	1831	7442	7431	16829	16810
22-21	1591	1586	6449	6438	14584	14563
23-22			5626	5613	12721	12698
24-23			4937	4923	11163	11138
25-24			4356	4341	9849	9822
26-25			3863	3847	8733	8704
27-26			3442	3424	7780	7750
28-27			3079	3061	6961	6928
29-28			2766	2746	6253	6219
30-29			2494	2473	5638	5602
31-30			2257	2235	5101	5063
32-31			2048	2025	4630	4591
33-32			1865	1841	4215	4174
34-33			1703	1678	3849	3806
35-34			1558	1532	3523	3478
36-35					3233	3186
37-36					2974	2925
38-37					2743	2693

number of electrons. In the lightest elements like neon, such electronic radiation falls below the detection threshold as is the case for the L series in argon.

X-ray emission in general is expected to increase strongly with nuclear charge Z because of the increasing fluorescence. Therefore, electronic X-rays have been observed mainly in heavy muonic and pionic atoms and in some cases from their energy shifts information on the ionisation state has been deduced [11, 26, 27, 28, 29]. Significant or even complete depletion of the electron shells, however, is only possible for light nuclei together with dilute targets [14, 30, 31]. In solid targets, in particular in the case of metals, due to instant refilling the exotic-atom cascade proceeds more or less in the presence of the electron shells as seen from a $K\alpha$ -to- $K\beta$ ratio as expected from an electronic $Z - 1$ atom [11].

In this paper we discuss the case of the noble gases argon, krypton, and xenon, i. e., for electron shells originally

occupied with 18, 36, and 54 electrons, the possible origin of the additional transitions in the energy range of fluorescence X-rays and their relation to the antiprotonic state during the atomic cascade. At pressures around 20 mbar the collision rate for, e. g., thermalised $\bar{p}\text{Ar}$ is estimated to about $3 \cdot 10^6/\text{s}$, whereas cascade times are 10^{-9}s or less. So electron refilling is strongly suppressed.

A short discussion of electronic X-rays emitted during the antiprotonic cascade was given by Bacher [22, 32] and Simons [23]. For the present analysis higher statistics measurements have been used and the electronic and antiprotonic binding energies have been calculated in Multi-configuration Dirac-Fock (MCDF) approximation including radiative and nuclear finite size corrections by using the code of Indelicato and Desclaux [33].

For the low-lying atomic levels strong interaction leads to a state dependent energy shift and level broadening. The highest circular states ($n_{\bar{p}}, \ell_{\bar{p}} = n_{\bar{p}} - 1$) affected by annihilation of antiprotons for atoms with $Z = 10, 18, 36$, and 54 are $(n_{\bar{p}}, \ell_{\bar{p}}) = (4, 3), (5, 4), (7, 6)$, and $(8, 7)$, respectively [34]. Transitions affected by strong interaction are not considered here.

2 Experiment

The X-ray spectra were measured at an extracted beam of the Low-Energy Antiproton Ring (LEAR) at CERN by using the set-up of LEAR experiment PS175, the main goal of which was the determination of strong-interaction effects in antiprotonic hydrogen and helium isotopes formed at low densities [35, 36, 37, 38]. The set-up, which included the cyclotron trap, allowed to stop up to 90% of the 105 MeV/c antiproton beam in a gaseous target of a few tens of mbar pressure in a volume of about 20 cm³ only. The X-rays were detected with a Si(Li) detector of 30 mm² inner area surrounded by a 200 mm² outer area, which was used in anticoincidence for background reduction (guard-ring configuration). The detector was located 16 cm away from the stop volume. In-beam energy resolution of the detector was measured to be 280 eV at 6.4 keV. Details about the experimental set-up may be found in [36, 37, 38].

In-beam detection efficiency and resolution have been determined from the saturated circular transitions of fully stripped low- Z antiprotonic systems like $\bar{p}\text{Ne}$ [22, 23] up to an energy of 30 keV (Fig. 3). For higher energies the efficiency is calculated from the conversion probability in 3.5 mm silicon given by the photo cross section [39]. A general feature of all X-ray spectra is an increasing background towards lower energies caused by the electromagnetic showers induced by the annihilation products in the surrounding materials.

3 Antiprotonic cascade in the presence of electrons

The initial de-excitation of the captured antiproton is dominated by $\Delta n_{\bar{p}} = 1$ E1 Auger emission of s electrons

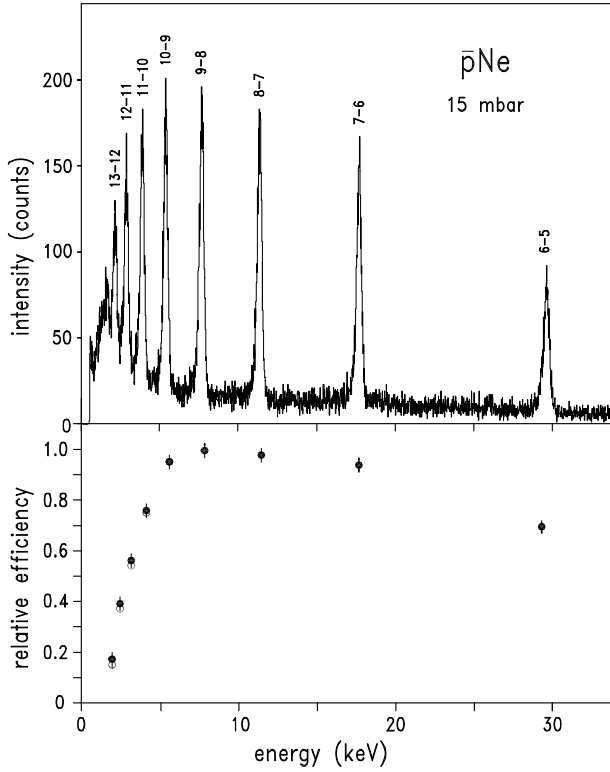


Fig. 3. Top – Antiprotonic neon as measured with a 30/200 mm² Si(Li) guard-ring detector. The relative detector efficiency is given by the line intensities because of the saturated line yields. Bottom – Relative detection efficiency as derived from the saturated lines of the $\bar{p}\text{Ne}$ spectrum. The upper points (full symbols) are due to the correction of self-absorption of X-rays in neon.

whenever energetically possible [18,19]. The general behaviour is easily deduced from an inspection of Ferrell's formula [40]

$$\Gamma_A/\Gamma_X = \sigma_{\gamma_e}^{(Z_{eff}^e-1)}(E)/[(Z_{eff}^e-1)^2\sigma_T], \quad (1)$$

which relates the ratio of Auger emission and X-ray transition rate to the energy dependence of the photoelectric cross section (Fig. 4). Here, $\sigma_{\gamma_e}(E)$ and σ_T denote the photoelectric and the Thomson cross sections. Z_{eff}^e is the effective charge seen by the electron. Reducing Z_{eff}^e by one unit takes into account the screening caused by the antiproton's charge.

Because the radiative decay width $\Gamma_X \propto \Delta E^3$ has a strong energy dependence, $\Delta n_{\bar{p}} > 1$ radiative transitions from low angular momentum states ℓ compete with Auger de-excitation. Hence, radiative transitions tend to populate circular states ($n_{\bar{p}}, \ell = n_{\bar{p}} - 1$), whereas $\Delta n_{\bar{p}} = 1$ Auger transitions leave the distribution of angular momentum states essentially unchanged. For large initial values $n_{\bar{p}}$ the energy gain for the $\Delta n_{\bar{p}} = 1$ transition favoured by the Auger process ($\Gamma_A \propto 1/\sqrt{E}$) is not sufficient for ionisation. Hence, it is expected that $\Delta n_{\bar{p}} > 1$ Auger transitions are also important.

As the Auger process depletes the electronic shells, the reduced screening of the nuclear charge increases the binding energy of the remaining electrons. Whenever the binding energy becomes larger than the antiprotonic transition energy, Auger de-excitation is interrupted (*effective stoppage of energy loss*: [13]) or even stopped when all atomic electrons are ejected. Hereafter the exotic atom loses energy only through $\Delta n_{\bar{p}} \geq 1$ radiative transitions, enhancing further the population of states with $(n_{\bar{p}}, n_{\bar{p}} - 1)$ from where the cascade can continue only via circular transitions ($n_{\bar{p}}, \ell_{\bar{p}} = n_{\bar{p}} - 1 \rightarrow (n_{\bar{p}} - 1, \ell_{\bar{p}} = n_{\bar{p}} - 2)$). The higher weight of the states with large angular momentum ℓ in addition enhances the development of a circular cascade. For $Z = 2$ such a limitation to radiative de-excitation between high-lying circular states leads to metastability [41] because of suppression of $\Delta n_{\bar{p}}, \Delta \ell_{\bar{p}} > 1$ Auger transitions [42] and is observed by a significantly increased cascade time of a fraction of the formed $\bar{p}\text{He}$ atoms [43].

The large initial value of $n_{\bar{p}}$ allows a large number of de-excitation steps, which leads very soon to an almost circular cascade and, up to krypton, to a complete removal of all electrons if refilling is avoided [22]. Hence, in dilute targets low and medium- Z antiprotonic atoms exist as true hydrogen-like systems during the intermediate cascade. In the case of xenon, however, the non-saturation of the X-ray yields for initial states $n_{\bar{p}} \leq 14$ indicates that

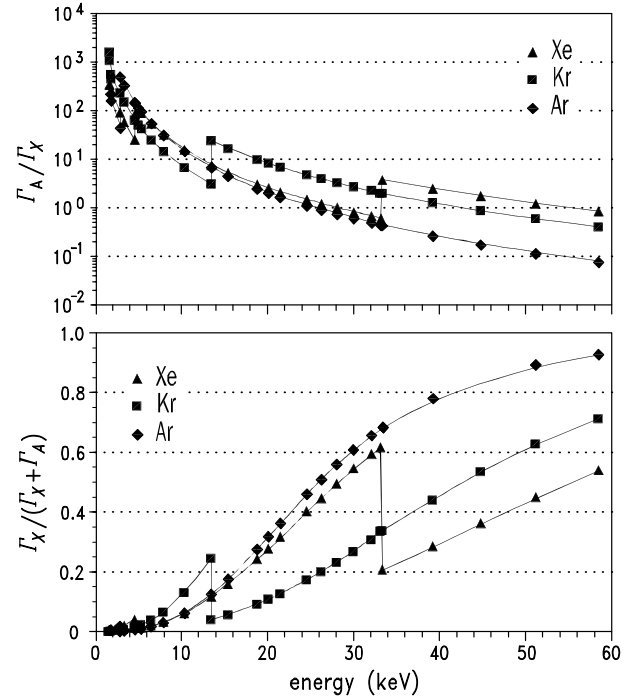


Fig. 4. Top – relative strength of Auger to radiative de-excitation as calculated from Ferrell's formula for fully occupied electron shells [22]. Here $Z_{eff}^e = Z - 1$ is taken, which corresponds to an antiproton already inside the electronic K shell. Bottom – relative strength of X-ray to total de-excitation. In the case the electron's binding energy is larger than the energy gain of the antiprotonic transition, Auger emission is suppressed.

the number of steps is not sufficient for complete removal of 54 electrons. Details are discussed in Sec. 3.

We characterize the complex interplay between the antiproton and the electron shells by the antiprotonic quantum number $n_{\bar{p}}$, the number of electrons present at that stage, and their binding energies. When discussing a cascade dominated by circular transitions, i.e., $\ell_{\bar{p}} = n_{\bar{p}} - 1$, and in addition $\ell_{\bar{p}} \gg 1$, the antiproton's probability density is finite only around a rather well defined distance $R_{\bar{p}}$ from the nucleus. Its binding energy is determined by $n_{\bar{p}}$ and the effective nuclear charge $Z_{eff}^{\bar{p}}$, where $Z_{eff}^{\bar{p}}$ depends on both the distance $R_{\bar{p}}$ and on the number of remaining electrons, which in turn is related to the level reached by the antiproton. Therefore, the quantities $n_{\bar{p}}$, $Z_{eff}^{\bar{p}}$, $R_{\bar{p}}$, and number of electrons are strongly correlated.

To obtain a qualitative description of this correlation, the dependence of $Z_{eff}^{\bar{p}}$ on the root mean square radius $R_{\bar{p}}$ is computed for the electronic K, L, M, N, and O shells by using the MCDF code. From these values a continuous function $Z_{eff}^{\bar{p}}(R_{\bar{p}})$ is constructed by interpolation. We obtain for argon, krypton, and xenon

$$Z_{eff}^{\bar{p}Ar}(R_{\bar{p}}) = 18.174e^{-0.534 \cdot R_{\bar{p}}}, \quad (2)$$

$$Z_{eff}^{\bar{p}Kr}(R_{\bar{p}}) = 36.167e^{-0.579 \cdot R_{\bar{p}}}, \text{ and} \quad (3)$$

$$Z_{eff}^{\bar{p}Xe}(R_{\bar{p}}) = 54.237e^{-0.8654 \cdot R_{\bar{p}} + 0.002287 \cdot R_{\bar{p}}^2 + 0.069956 \cdot R_{\bar{p}}^3} \quad (4)$$

To calculate the (non-relativistic) transition energies $\Delta E_{n_{\bar{p}} \rightarrow n_{\bar{p}}-1}$ we start at a value of $R_{\bar{p}}$ that corresponds to the outermost shell of electrons, where about the quantum cascade is expected to start. The corresponding radial quantum number $n_{\bar{p}}$ is then given by

$$n_{\bar{p}} = \sqrt{R_{\bar{p}} \cdot Z_{eff}^{\bar{p}} \cdot m_{\bar{p}}/m_e} \quad (5)$$

and the antiprotonic transition energy for $n_{\bar{p}} \rightarrow n_{\bar{p}} - 1$ by

$$\Delta E_{n_{\bar{p}} \rightarrow n_{\bar{p}}-1} = E_{Ryd} \cdot \frac{(Z_{eff}^{\bar{p}})^2 (2n_{\bar{p}} - 1)}{[n_{\bar{p}}(n_{\bar{p}} - 1)]^2} \quad (6)$$

with the antiprotonic Rydberg energy $E_{Ryd} = m_{\bar{p}} c^2 \alpha^2 / 2 = 24982.2 \text{ eV}$. $R_{\bar{p}}$ for $n_{\bar{p}} - 1$ is calculated from equation (5), which yields the corresponding $Z_{eff}^{\bar{p}}$ by using the expressions (2)–(4). Inserting the new values for $Z_{eff}^{\bar{p}}$ the energy of the next lower transition is obtained from (6). This procedure is repeatedly applied. The approximations made here are regarded to be sufficient in view of the complexity of the cascade processes. The results are given in Tables 2–4 along with the electronic binding energies for the successive states of ionisation. For each pair of $n_{\bar{p}}$ and $Z_{eff}^{\bar{p}}$ the relativistic transition energy is then calculated with the MCDF code. The large mass of the antiproton leads to much smaller radii and, consequently, the effect of electron screening is reduced for the observable transitions as compared to muonic or pionic atoms [44, 45, 46].

In Fig. 5 the results for antiprotonic transition, electronic binding energy, and antiproton and electron orbits are combined. One finds that the maximum probability

density of antiproton and electron do not overlap when ionization occurs by $\Delta n_{\bar{p}} = 1$ transitions. The antiproton has to be always far inside the corresponding electron shell.

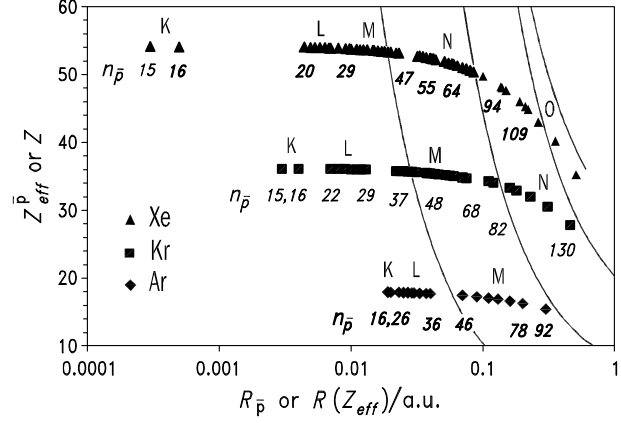


Fig. 5. Effective nuclear charge $Z_{eff}^{\bar{p}}$ acting on the antiproton as a function of its distance $R_{\bar{p}}$. K, L, M, N, and O indicate the regions where these shells can be ionised by antiprotonic $\Delta n_{\bar{p}} = 1$ transitions. Solid lines show the average radii of the electron shells K, L, M1–M3, and M4–M5 (from left) for the screened nuclear charge Z . The different screening for the various subshells is taken into account by the shielding constants Z_{shell}^S ($Z_K^S = 0.3$, $Z_L^S = 4.15$, $Z_{M1-M3}^S = 11.25$, and $Z_{M4-M5}^S = 21.15$ [47].)

Vice versa, the presence of the antiproton inside the electron cloud reduces the electronic binding energies. Because of its large mass the orbit is rather well localised for $\ell \gg 1$ states and, therefore, it shields the nuclear charge by almost one unit for all electron shells outside its orbit. Binding energy and effective charge Z_{eff}^e for varying number of electrons for argon, krypton, and xenon are given in Tables 5–7. With the use of these tables, we shall describe the main features of the antiprotonic cascade in the presence of electrons. Although the qualitative picture is similar for these three elements, a quantitative description shows that differences observed can be attributed to the increasing number of electrons. To keep the following discussion transparent, we develop the features for a purely circular antiprotonic cascade.

3.1 Antiprotonic Cascade in Argon ($Z=18$)

Assuming capture in the spatial region of the 3s and 3p electrons, the effective charge seen by the antiproton is about $Z_{eff}^{\bar{p}} = 8$ and its binding energy is about 16 eV being equal to the ionisation potential of the most weakly bound electrons. According to the thumb rule with $n_e = 3$ the radial quantum number for the start of the quantum cascade reads $n_{\bar{p}} \approx 43 \cdot n_e = 128$. For $n_{\bar{p}} \approx 128$ the antiprotonic transition $n_{\bar{p}} \rightarrow n_{\bar{p}} - 1$ has an energy of about 5 eV only, whereas the binding energies of the 3s, 3p_{1/2}, and

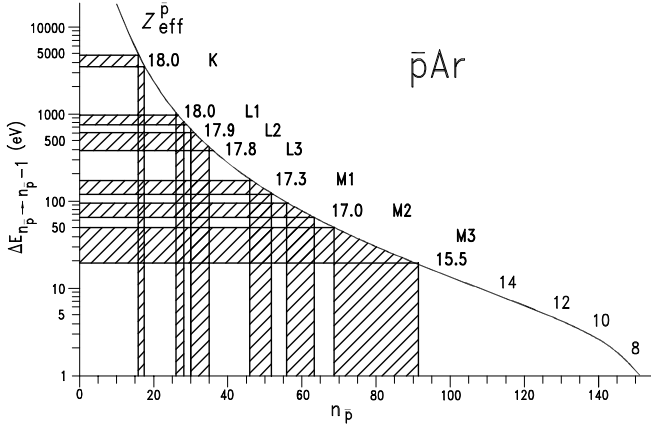


Fig. 6. Energies of circular $\Delta n_{\bar{p}} = 1$ transitions in antiprotonic argon. The effective charge $Z_{\text{eff}}^{\bar{p}}$ acting on the antiproton determines when depletion of the various electron shells starts. In the beginning, Z_{eff} varies strongly with the number of remaining electrons being about 15 when M-shell emission starts. For L-shell emission, the antiproton is already closer to the nucleus than any electron. Hence, Z_{eff} approaches the value of the unscreened nuclear charge of 18.

$3p_{3/2}$ electrons are 35, 16.2 and 16.0 eV, respectively (Table 5). Consequently the antiproton must descend the cascade ladder by radiative transitions until it gains enough energy to remove the M electrons or the cascade has to start at somewhat lower-lying states. Figure 6 shows the range for the quantum number $n_{\bar{p}}$, where Auger emission is allowed in $\Delta n_{\bar{p}} = 1$ transitions for the various electron shells.

In the region of the L electrons ($n_{\bar{p}} \approx 80$) $Z_{\text{eff}}^{\bar{p}}$ has increased to about 15. Around $n_{\bar{p}} = 80$ the antiprotonic transition energies amount to 20–50 eV, which is now sufficient to remove the M3 electrons (Table 2 and Fig. 6). After complete depletion of the M shell, arriving at the ionisation state Ar^{8+} , the antiproton is situated well inside the L shell. Because of the screening of one nuclear charge by the antiproton, the electronic L shell experiences rather the Coulomb field of a Cl^{7+} ion. The binding energy for one electron in a full L shell is 350 eV.

In the region of the K electrons, $Z_{\text{eff}}^{\bar{p}}$ for the antiproton exceeds already 17. At $n_{\bar{p}} \approx 35$ the energy of a circular transition reaches 350 eV now being able to remove L electrons. After removal of the L shell, the argon atom is highly ionized ($\text{p}\bar{\text{Ar}}^{16+} = \text{Cl}^{15+}$) with the antiproton far inside the K shell experiencing the full nuclear charge $Z = 18$. The screening of one nuclear charge by the antiproton reduces the electron binding energies of Ar^{16+} and Ar^{17+} from 4122 and 4427 eV for the $1s^2$ and $1s^1$ configurations to 3659 and 3947 eV, respectively. Removal of the first K electron by a circular transition is not yet possible for $\text{p}\bar{\text{Ar}}^{16+}$ (17–16). It requires 4 or more additional electrons in the L-shell. A single K electron (H-like “Cl”) can be removed first by the $\text{p}\bar{\text{Ar}}^{17+}$ (16–15) transition (4250 eV).

3.2 Antiprotonic Cascade in Krypton ($Z=36$)

In krypton, the antiprotonic cascade is assumed to start at about the electronic N shell. With $n_{\bar{p}} \approx 170$ and the effective charge $Z_{\text{eff}}^{\bar{p}} \approx 25$ circular transitions in this region have energies around 7 eV. The binding energies of 4s and 4p electrons are 32 and 15 eV, respectively (Table 6). The calculations of electronic and antiprotonic orbital energies and radii show that step by step ionisation of the $4p_{3/2}$, $4p_{1/2}$ and 4s electrons by $\Delta n_{\bar{p}} = 1$ transitions happens for $Z_{\text{eff}}^{\bar{p}} \approx 28 - 34$ corresponding to $n_{\bar{p}} \approx 150 - 82$ (Table 3 and Fig. 7). At this stage the antiproton finds itself within the L shell and just about outside the K shell. The absence of the screening by the N electrons increases the binding energy of the M shell for 3s, 3p, and 3d electrons from 305, 230, and 102 eV to 438, 363, and 235 eV, respectively. With the antiproton inside the M shell, the effective charge for M electrons is lowered by one unit and so the binding energies are reduced by about 3.7%.

The transitions ($n_{\bar{p}} \rightarrow n_{\bar{p}} - 1$) for $n_{\bar{p}} = 68$ to $n_{\bar{p}} = 48$ have sufficient energy to remove the M electrons leaving the krypton atom in a state $\text{p}\bar{\text{Kr}}^{26+} = \text{Br}^{25+}$. For this ionisation state the L-electron binding energies increase substantially by 53% for 2s and 60% for 2p compared to the neutral atom (Table 6).

After crossing the electron K shell the antiproton sees almost the full nuclear charge of $Z = 36$. The antiprotonic transitions from $n_{\bar{p}} = 29$ to 22 are able to remove the L electrons successively. So when the antiproton reaches $n_{\bar{p}} = 17$ the krypton atom is expected to possess only K electrons. The K electrons now have a binding energy of 16341 eV for the $1s^2$ and 16960 eV for the $1s^1$ configurations being 13% and 17.5% larger than for neutral krypton. Circular transitions starting from $n_{\bar{p}} \leq 16$ can now ionise any K electron.

From this analysis, we infer that the $\Delta n = 1$ antiprotonic transitions, having enough energy to ionize the N-, M-, L-, and K-shell electrons, start at $n_{\bar{p}} \approx 150, 68, 29$, and 16, respectively, with a corresponding nuclear charge of $Z_{\text{eff}}^{\bar{p}} = 28, 35, 35.9$, and 36 (Fig. 7). After complete removal of the M electrons, the antiproton has reached the spatial region of the electronic K shell, i. e., $n_{\bar{p}} \approx 40$ with $Z_{\text{eff}}^{\bar{p}} \approx 36$. This means, that, although the maximum spa-

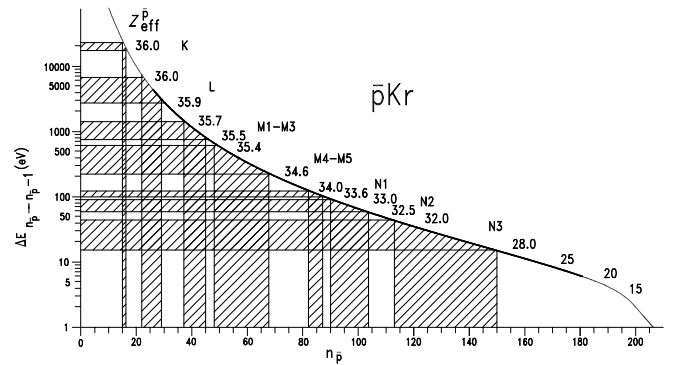


Fig. 7. Energies of $\Delta n_{\bar{p}} = 1$ transitions in antiprotonic krypton.

Table 2. State and cascade dependent ionisation energies in antiprotonic argon calculated by MCDF. $R_{\bar{p}}$ is a measure for the distance of the antiproton to nucleus (one a.u.= $0.53 \cdot 10^{-10}$ m) and $Z_{eff}^{\bar{p}}$ the actual nuclear charge screened by the electrons. For example, the first antiprotonic $\Delta n_{\bar{p}} = 1$ de-excitation step being able to ionise the first 2s electron ($E_B = 748$ eV) is the (27–26) transition ($\Delta E_{n_{\bar{p}} \rightarrow n_{\bar{p}}-1} = 850$ eV). Dots (...) denote fully occupied lower-lying electron states.

electronic state	no. of electrons	$R_{\bar{p}}$ / a. u.	$Z_{eff}^{\bar{p}}(n_{\bar{p}})$	$n_{\bar{p}}$	$\Delta E(Z_{eff}^{\bar{p}})$ $n_{\bar{p}} \rightarrow n_{\bar{p}} - 1$	ionisation energy (MCDF)		
						$Z^e = 18$ / eV	$Z^e = 18 + \bar{p}$ / eV	$Z^e = 17$ / eV
$1s^2 2s^2 2p^6 3s^2 3p^6$	18					16	capture of \bar{p}	
$\dots 3s^2 (3p_{1/2})^2 (3p_{3/2})^3$	17	0.3	15.49	92	21	28	15	14
$\dots 3s^2 (3p_{1/2})^2 (3p_{3/2})^2$	16	0.2	16.29	78	36	42	26	25
$\dots 3s^2 (3p_{1/2})^2 (3p_{3/2})^1$	15	0.16	16.72	69	52	42	26	25
$\dots 3s^2 (3p_{1/2})^2$	14	0.13	16.97	63	67	74	57	53
$\dots 3s^2 (3p_{1/2})^1$	13	0.11	17.23	56	96	90	71	67
$\dots (3s_{1/2})^2$	12	0.09	17.36	52	120	122	100	95
$\dots (3s_{1/2})^1$	11	0.07	17.54	46	172	143	116	114
$1s^2 2s^2 (2p_{1/2})^2 (2p_{3/2})^4$	10	0.040	17.81	35	392	424	351	346
$1s^2 2s^2 (2p_{1/2})^2 (2p_{3/2})^3$	9	0.037	17.83	34	427	484	405	400
$1s^2 2s^2 (2p_{1/2})^2 (2p_{3/2})^2$	8	0.033	17.87	32	515	547	467	452
$1s^2 2s^2 (2p_{1/2})^2 (2p_{3/2})^1$	7	0.030	17.91	30	628	622	537	527
$1s^2 2s^2 (2p_{1/2})^2$	6	0.029	17.92	29	698	689	599	594
$1s^2 2s^2 (2p_{1/2})^1$	5	0.027	17.94	28	779	754	661	655
$1s^2 (2s_{1/2})^2$	4	0.025	17.96	27	870	850	748	745
$1s^2 (2s_{1/2})^1$	3	0.023	17.97	26	978	918	812	809
$(1s_{1/2}^2)$	2	0.020	18	17	3520	4122	3663	3659
$(1s_{1/2}^1)$	1	0.019	18	16	4250	4427	3950	3947

tial overlap of the antiprotonic wave function with the K- and L-shell electrons occurs at $n_{\bar{p}} \approx 42$ and 84, respectively, $\Delta n_{\bar{p}} = 1$ transitions do not possess enough energy to ionise the L electrons. The L-shell ionisation takes place when the antiproton has reached $n_{\bar{p}} \approx 28$ with $Z_{eff}^{\bar{p}} \approx 36$. M- and N-shell ionisation show a similar behaviour. The effective charge seen by the M electrons is obtained from these calculations corrected by nearly one unit to take into account the screening by the antiproton's charge (Table 6).

3.3 Antiprotonic Cascade in Xenon ($Z=54$)

The antiprotonic cascade in xenon is more complex than that of argon and krypton because of the larger number of electrons. Assuming that it starts at about $n_e = 5$ the effective charge acting on the 5s and 5p electrons is $Z_{eff}^e \approx 20$ and 15, respectively (Table 7). The $\Delta n_{\bar{p}} = 1$ transitions that possess sufficient energy to ionise O-shell electrons with binding energies of 12–27 eV will start at $n_{\bar{p}} \cong 180$ where $Z_{eff}^{\bar{p}} \approx 5$ (Fig. 8 and Table 4). During antiproton capture it is likely that due to shake-off effects more than one electron is emitted from the $n_e = 5$ shell. In the absence of only one 5p electron the binding energy of 5s increases by 16 eV and $Z_{eff}^{\bar{p}}$ to 16.5. This means that the antiproton has to reach $n_{\bar{p}} = 87$ to remove a 5s electron by a circular transition.

In Fig. 8 the antiprotonic transition energies ($n_{\bar{p}} \rightarrow n_{\bar{p}} - 1$) are given for specific values of $Z_{eff}^{\bar{p}}$. With an empty O shell the binding energy of 4d electrons increases to 71 eV and the antiproton has to descend to $n_{\bar{p}} \approx 90$

with $Z_{eff}^{\bar{p}} \approx 50$ to ionise 4d electrons by $\Delta n_{\bar{p}} = 1$ Auger emission. At $n_{\bar{p}} \approx 55$ the last N electron may be removed and the xenon atom is 26-fold ionised.

After removal of the N electrons the antiproton has crossed the electronic L and M shell and is about to enter the K shell. The binding energy of the M electrons increases to 1413 and 1401 eV for electronic $3d_{3/2}$ and $3d_{5/2}$ states, respectively. Ionisation of the M shell by circular transitions starts at $n_{\bar{p}} = 47$ and $Z_{eff}^{\bar{p}} \approx 53$. When reaching $n_{\bar{p}} \approx 29$ the M shell may be completely ionised. The antiproton, being now far inside the K shell, experiences the full nuclear charge independent of the status of the electron shell.

With only L and K shells remaining, the $\bar{p}\text{Xe}$ atom is 44-fold ionised and the electron binding energy of the $2p_{3/2}$, $2p_{1/2}$, and 2s state increases to 7340, 7647, and 7946 eV, respectively. Auger emission by $\Delta n_{\bar{p}} = 1$ starts at $n_{\bar{p}} = 27$, where the antiproton's circular transition of 7780 eV exceeds the electronic binding energy of 7340 eV (see Table 1). When the antiproton reaches $n_{\bar{p}} = 22$ the L shell may be completely depleted.

In the case that such a 52-fold ionised state is reached, the K-electron binding energies for the $1s^2$ and the $1s^1$ configurations become 40271 and 41300 eV. Screening of one charge unit by the antiproton reduces these energies by 2.9% to 38793 and 39785 eV. The antiprotonic transition 16–15 having the energy of 39028 eV is able to eject one K electron only if the second one is still present.

Table 3. State and cascade dependent ionisation energies in antiprotonic krypton.

electronic state	no. of electrons	$R_{\bar{p}}$	$Z_{eff}^{\bar{p}}(n_{\bar{p}})$	$n_{\bar{p}}$	$\Delta E(Z_{eff}^{\bar{p}})$ $n_{\bar{p}} \rightarrow n_{\bar{p}} - 1$	ionisation energy (MCDF)		
		/ a. u.				$Z^e = 36$ / eV	$Z^e = 36 + \bar{p}$ / eV	$Z^e = 35$ / eV
$\dots 4s^2(4p_{1/2})^2(4p_{3/2})^4$	36					13	capture of \bar{p}	
$\dots 4s^2(4p_{1/2})^2(4p_{3/2})^3$	35	0.46	28	150	16	24	11	11
$\dots 4s^2(4p_{1/2})^2(4p_{3/2})^2$	34	0.31	30	130	30	34	20	20
$\dots 4s^2(4p_{1/2})^2(4p_{3/2})^1$	33	0.23	32	113	46	50	35	34
$\dots 4s^2(4p_{1/2})^2$	32	0.18	32.5	104	60	64	47	46
$\dots 4s^2(4p_{1/2})^1$	31	0.16	33.0	90	88	77	61	59
$\dots 4s_{1/2})^2$	30	0.12	33.6	87	101	106	86	85
$\dots 4s_{1/2})^1$	29	0.11	34.0	82	119	124	103	102
$\dots (3d_{3/2})^4(3d_{5/2})^6$	28	0.075	34.68	68	211	231	191	191
$\dots (3d_{3/2})^4(3d_{5/2})^5$	27	0.070	34.85	64	253	272	229	229
$\dots (3d_{3/2})^4(3d_{5/2})^4$	26	0.060	34.93	62	278	302	257	257
$\dots (3d_{3/2})^4(3d_{5/2})^3$	25	0.056	35.05	59	323	348	300	300
$\dots (3d_{3/2})^4(3d_{5/2})^2$	24	0.052	35.13	57	359	388	338	337
$\dots (3d_{3/2})^4(3d_{5/2})^1$	23	0.046	35.23	54	418	446	395	393
$\dots (3d_{3/2})^4$	22	0.043	35.27	52	468	491	436	435
$\dots (3d_{3/2})^3$	21	0.040	35.33	50	527	546	489	488
$\dots (3d_{3/2})^2$	20	0.038	35.37	49	560	584	525	524
$\dots (3d_{3/2})^1$	19	0.037	35.41	48	597	639	578	577
$\dots 3s^2(3p_{1/2})^2(3p_{3/2})^4$	18	0.031	35.52	45	732	784	716	715
$\dots 3s^2(3p_{1/2})^2(3p_{3/2})^3$	17	0.029	35.55	44	785	837	767	766
$\dots 3s^2(3p_{1/2})^2(3p_{3/2})^2$	16	0.028	35.56	43	843	875	804	803
$\dots 3s^2(3p_{1/2})^2(3p_{3/2})^1$	15	0.027	35.60	42	994	936	862	861
$\dots 3s^2(3p_{1/2})^2$	14	0.025	35.63	40	1108	996	919	918
$\dots 3s^2(3p_{1/2})^1$	13	0.024	35.66	39	1192	1050	970	969
$\dots (3s_{1/2})^2$	12	0.023	35.68	38	1225	1150	1067	1066
$\dots (3s_{1/2})^1$	11	0.022	35.71	37	1327	1204	1119	1118
$1s^2 2s^2(2p_{1/2})^2(2p_{3/2})^4$	10	0.013	35.88	29	2790	2972	2732	2728
$1s^2 2s^2(2p_{1/2})^2(2p_{3/2})^3$	9	0.012	35.90	28	3108	2924	2892	2887
$1s^2 2s^2(2p_{1/2})^2(2p_{3/2})^2$	8	0.011	35.92	27	3473	3089	3002	2997
$1s^2 2s^2(2p_{1/2})^2(2p_{3/2})^1$	7	0.010	35.94	26	3902	3203	3202	3168
$1s^2 2s^2(2p_{1/2})^2$	6	0.009	35.96	25	4402	3380	3371	3366
$1s^2 2s^2(2p_{1/2})^1$	5	0.009	35.97	24	4587	3590	3532	3527
$1s^2(2s_{1/2})^2$	4	0.008	35.98	23	5683	3756	3733	3728
$1s^2(2s_{1/2})^1$	3	0.007	36	22	6585	3963	3875	3869
$(1s_{1/2}^2)$	2	0.004	36	16	17248	17309	16341	16315
$(1s_{1/2}^1)$	1	0.003	36	15	21081	17959	16960	16937

4 Discussion of the spectra

4.1 Antiprotonic Argon

The antiprotonic argon X-ray spectrum (Fig. 2) is dominated by saturated circular transitions. The decrease in intensity below 3 keV and towards high energies is due to the detection efficiency (Fig. 3). The gap between the strong transitions (18–17) and (15–14) is attributed to K electron emission (Fig. 9). Such a gap is not observable in $\bar{p}\text{Ne}$ because it is below the detection threshold. As discussed in Sec. 3.1 for a circular cascade, the antiproton is able to ionise the argon atom up to the state where only the K electrons remain when it reaches $n_{\bar{p}} \cong 25$ (Table 2).

The intensity of the $\bar{p}\text{Ar}(16\text{--}15)$ line suggests about 25% completely ionised argon for states with $n_{\bar{p}} > 17$ (Ta-

ble 9). Such a high ionisation requires $\Delta n_{\bar{p}} \geq 2$ transitions in the upper part of the cascade, but with not too small angular momenta, because otherwise $\Delta n_{\bar{p}} \gg 1$ radiative de-excitation dominates over Auger emission.

The $\bar{p}\text{Ar}(17\text{--}16)$ transition energy strongly depends on the ionisation state. As can be seen from Table 5, the $\bar{p}\text{Ar}(17\text{--}16)$ transition is not able to ionise a K electron in the case that only 3 or less electrons are present. On the other hand any L electron would be ejected by preceeding circular transitions. However, inner transitions ($\Delta n_{\bar{p}} > 1, \ell \ll \ell_{max}$) are able to reach the $n_{\bar{p}} = 17$ state with L electrons still present. Ejection of the second K electron could proceed via the $\bar{p}\text{Ar}(15\text{--}14)$ line, which indeed is weakened by 10–20% as compared to the following transitions. From the $\bar{p}\text{Ar}(14\text{--}13)$ line onwards the transi-

Table 4. State and cascade dependent ionisation energies in antiprotonic xenon.

electronic state	no. of electrons	$R_{\bar{p}}$	$Z_{eff}^{\bar{p}}(n_{\bar{p}})$	$n_{\bar{p}}$	$\Delta E(Z_{eff}^{\bar{p}})$ $n_{\bar{p}} \rightarrow n_{\bar{p}} - 1$	ionisation energy (MCDF)		
		/ a. u.				$Z^e = 54$ / eV	$Z^e = 54 + \bar{p}$ / eV	$Z^e = 53$ / eV
$\dots 5s^2(5p_{1/2})^2(5p_{3/2})^4$	54					11	capture of \bar{p}	
$\dots 5s^2(5p_{1/2})^2(5p_{3/2})^{1-3}$	51–53	0.22–0.51	43–40	144–180		42–21	31–11	29–10
$\dots 5s^2(5p_{1/2})^{1,2}$	49,50	0.19,0.22	46,45	126,134		66,54	53,42	51,40
$\dots (5s_{1/2})^{1-2}$	47,48	0.14,0.15	48.2,47.4	109,115		104,90	88,74	86,72
$\dots (4d_{5/2})^{1-6}$	41–46	0.064–0.10	51.3–49.8	77–94		314–178	284–154	279–150
$\dots (4d_{3/2})^{1-4}$	37–40	0.051–0.060	51.9–51.4	69–75		434–344	399–312	393–307
$\dots 4s^2(4p_{1/2})^2(4p_{3/2})^4$	36	0.044	52.27	64	631	550	510	504
$\dots 4s^2(4p_{1/2})^2(4p_{3/2})^3$	35	0.042	52.33	63	653	587	546	540
$\dots 4s^2(4p_{1/2})^2(4p_{3/2})^2$	34	0.041	52.39	62	678	611	570	564
$\dots 4s^2(4p_{1/2})^2(4p_{3/2})^1$	33	0.040	52.45	61	706	650	608	602
$\dots 4s^2(4p_{1/2})^2$	32	0.037	52.57	59	764	700	654	648
$\dots 4s^2(4p_{1/2})^1$	31	0.035	52.63	58	795	736	689	683
$\dots 4s_{1/2}^2$	30	0.033	52.74	56	869	818	768	762
$\dots 4s_{1/2}^1$	29	0.032	52.79	55	912	856	805	799
$\dots (3d_{3/2})^4(3d_{5/2})^6$	28	0.023	53.18	47	1456	1494	1400	1397
$\dots (3d_{3/2})^4(3d_{5/2})^5$	27	0.022	53.20	45	1660	1587	1489	1488
$\dots (3d_{3/2})^4(3d_{5/2})^4$	26	0.021	53.27	44	1780	1647	1548	1547
$\dots (3d_{3/2})^4(3d_{5/2})^3$	25	0.020	53.30	43	1896	1742	1640	1639
$\dots (3d_{3/2})^4(3d_{5/2})^2$	24	0.019	53.35	42	2038	1815	1711	1710
$\dots (3d_{3/2})^4(3d_{5/2})^1$	23	0.018	53.40	41	2195	1919	1813	1812
$\dots (3d_{3/2})^4$	22	0.017	53.43	40	2367	2023	1913	1913
$\dots (3d_{3/2})^3$	21	0.016	53.48	39	2559	2127	2014	2014
$\dots (3d_{3/2})^2$	20	0.015	53.50	38	2770	2195	2080	2079
$\dots (3d_{3/2})^1$	19	0.0146	53.55	37	2986	2300	2082	2181
$\dots 3s^2(3p_{1/2})^2(3p_{3/2})^4$	18	0.0140	53.59	36	3250	2556	2432	2431
$\dots 3s^2(3p_{1/2})^2(3p_{3/2})^3$	17	0.0132	53.62	35	3547	2651	2525	2524
$\dots 3s^2(3p_{1/2})^2(3p_{3/2})^2$	16	0.0124	53.66	34	3873	2713	2585	2584
$\dots 3s^2(3p_{1/2})^2(3p_{3/2})^1$	15	0.0117	53.69	33	4247	2811	2681	2680
$\dots 3s^2(3p_{1/2})^2$	14	0.0110	53.72	32	4664	2975	2838	2836
$\dots 3s^2(3p_{1/2})^1$	13	0.0100	53.75	31	5142	3068	2928	2926
$\dots (3s_{1/2})^2$	12	0.0097	53.78	30	5687	3242	3098	3096
$\dots (3s_{1/2})^1$	11	0.0091	53.81	29	6413	3333	3186	3184
$1s^2 2s^2(2p_{1/2})^2(2p_{3/2})^4$	10	0.0080	53.87	27	7821	7660	7340	7338
$1s^2 2s^2(2p_{1/2})^2(2p_{3/2})^3$	9	0.0070	53.89	26	8783	7931	7604	7602
$1s^2 2s^2(2p_{1/2})^2(2p_{3/2})^2$	8	0.0068	53.91	25	9909	8103	7774	7772
$1s^2 2s^2(2p_{1/2})^2(2p_{3/2})^1$	7	0.0063	53.94	24	11139	8382	8046	8044
$1s^2 2s^2(2p_{1/2})^2$	6	0.0058	53.96	23	12812	8971	8604	8601
$1s^2 2s^2(2p_{1/2})^1$	5	0.0053	53.98	22	14726	9243	8869	8866
$1s^2(2s_{1/2})^2$	4	0.0049	54	21	16827	9580	9200	9196
$1s^2(2s_{1/2})^1$	3	0.0044	54	20	19557	9810	9425	9421
$(1s_{1/2}^2)$	2	0.0005	54	16	39028	40269	38719	38715
$(1s_{1/2}^1)$	1	0.0003	54	15	47708	41300	41300	39722

tions are consistent with a pure radiative cascade without any Auger component and the $\bar{p}\text{Ar}$ atom exists as a pure hydrogen-like system.

Because of its high yield the line at the $\bar{p}\text{Ar}(18-17)$ position is interpreted as a superposition of argon $K\alpha$ fluorescence radiation and the antiprotonic line (Table 8). The energy of the electronic X-rays is consistent with low charge states only. As no $K\beta$ component has been found, a significant direct ionisation by the beam is excluded. The

high yield of the transition at the energy of the $\bar{p}\text{Ar}(19-18)$ remains unexplained. A possible reason maybe an improper treatment of the background.

At 3.77 keV an additional transition is detected, which appears with an intensity comparable to the $\bar{p}\text{Ar}(17-16)$ transition. As can be seen from Table 5 it cannot be attributed to an electronic $2p-1s$ transition for any ionisation state or to a $\bar{p}\text{Ar}$ atom. Lines of low intensity were found at 7.2, 11.1, and 22.8 keV. The energies of the first

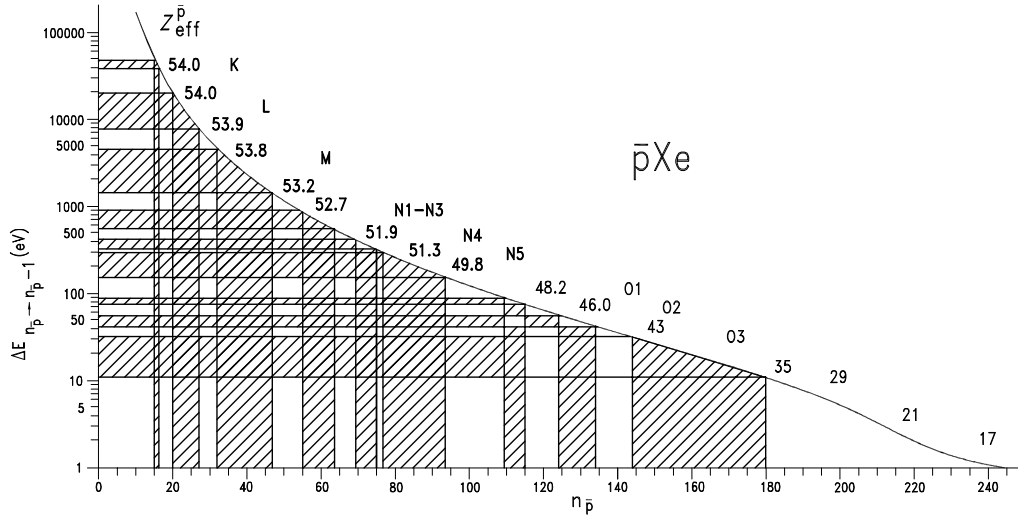


Fig. 8. Energies of $\Delta n_{\bar{p}} = 1$ transitions in antiprotonic xenon.

Table 5. Electron binding energies BE and effective nuclear charge Z_{eff}^e acting on the electrons of an Ar atom for different electronic configurations without and with (*in italic*) an antiproton present in a level $n_{\bar{p}}$ as indicated in the last row.

levels	$BE(eV)$	Z_{eff}^e	$BE(eV)$	Z_{eff}^e	$BE(eV)$	Z_{eff}^e	$BE(eV)$	Z_{eff}^e	$BE(eV)$	Z_{eff}^e	$BE(eV)$	Z_{eff}^e
1s	3239	17.4	3413	17.5	3747	17.5	3942	17.5	4122	17.6	4427	18.0
			<i>3001</i>	<i>16.4</i>	<i>3309</i>	<i>16.5</i>	<i>3490</i>	<i>16.6</i>	<i>3659</i>	<i>16.6</i>	<i>3947</i>	<i>17.0</i>
2s	337	14.6	500	13.5	724	15.9	850	16.4				
			<i>420</i>	<i>13.7</i>	<i>628</i>	<i>14.9</i>	<i>745</i>	<i>15.4</i>				
2p _{1/2}	262	13.4	426	13.5	687	15.2						
			<i>351</i>	<i>12.5</i>	<i>595</i>	<i>14.2</i>						
2p _{3/2}	260	13.3	425	13.5								
			<i>349</i>	<i>12.5</i>								
3s	35	9.5										
3p _{1/2}	16.2	7.5										
3p _{3/2}	16	7.5										
no. of electrons	18		10		6		4		2		1	
configuration	$1s^2 2s^2 2p^6 3s^2 3p^6$		$1s^2 2s^2 2p^6$		$1s^2 2s^2 2p^2$		$1s^2 2s^2$		$1s^2$		$1s^1$	
$n_{\bar{p}}$			15		15		15		15		15	

Table 8. Fluorescence X-rays from argon, krypton, and xenon and the corresponding $Z - 1$ atoms. The (experimental) energies are taken from [48].

	$K\alpha_1$	$K\alpha_2$	$K\beta_1$	$K\beta_3$	$L\alpha_1$	$L\beta_3$
Cl	2622.4	2620.9	2815.6			
Ar	2957.7	2955.6	3190.5			
Br	11924.4	11877.8	13291.6	13284.7	1480.5	
Kr	12648.0	12595.4	14112.8	14105.0	1585.4	
I	28612.3	28317.5	32295.1	32239.7	3937.7	4120.5
Xe	29778.8	29458.3	33624.2	33563.2	4110.1	4512.0

two lines coincide with $\bar{p}O(8-7)$ and $\bar{p}O(7-6)$ transitions originating from a small water contamination, whereas the

third one is not identified. No $\Delta n_{\bar{p}} = 2$ or 3 transitions could be identified in $\bar{p}Ar$.

4.2 Antiprotonic Krypton

The high energy part of the krypton spectrum shows a structure similar to that of argon (Fig. 2). The impossibility for the antiproton to eject K electrons by a circular transition at $n_{\bar{p}} > 16$ is evident from the saturated $\bar{p}Kr$ lines (23–22) to (17–16) followed by X-ray suppression for the (16–15) and (15–14) transitions. Due to the larger energies higher-lying antiprotonic transitions up to at least (25–24) become now visible. The intensity reduction for $n_{\bar{p}} \geq 26$ is due to the depletion of the L shell.

Additional intensity is observed in the energy range between 12 and 14 keV (Fig. 10). These lines are attributed in most of the cases to electronic X-rays (see below).

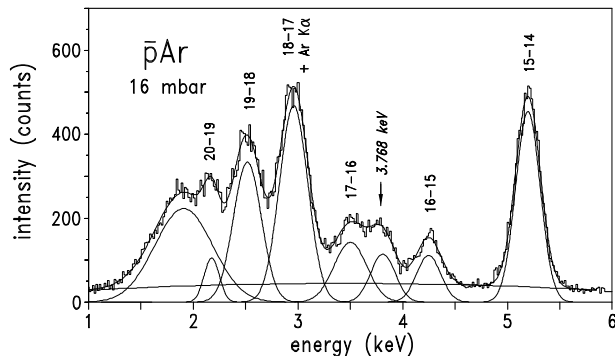
Table 6. Electron binding energies BE and effective nuclear charge Z_{eff}^e acting on the electrons of Kr. For explanation of symbols see Table 5.

levels	$BE(eV)$	Z_{eff}^e	$BE(eV)$	Z_{eff}^e	$BE(eV)$	Z_{eff}^e	$BE(eV)$	Z_{eff}^e	$BE(eV)$	Z_{eff}^e	$BE(eV)$	Z_{eff}^e
1s	14415	35.3	14532	35.3	15678	35.3	16922	35.6	17309	35.6	17949	36
					14750	34.3	15953	34.6	16328	34.6	16958	35
2s	1961	32.2	2096	32.2	3166	32.8	3965	34.6				
					2956	31.8	3729	33.5				
2p _{1/2}	1765	31.0	1899	31.0	2982	31.7						
					2779	30.7						
2p _{3/2}	1711	30.8	1846	30.8	2972	31.5						
					2730	30.5						
3s	305	25.4	438	25.4								
3p _{1/2}	234	23.3	367	23.4								
3p _{3/2}	226	23.0	359	23.2								
3d _{3/2}	103	19.0	236	19.5								
3d _{5/2}	101	18.9	235	19.4								
4s	32	15.0										
4p _{1/2}	15	12.0										
no. of electrons	36		28		10		4		2		1	
configuration	1s ² 2s ² 2p ⁶ 3s ² 3p ⁶ 3d ⁶ 4s ² 4p ⁶		1s ² 2s ² 2p ⁶ 3s ² 3p ⁶ 3d ⁶		1s ² 2s ² 2p ⁶		1s ² 2s ²		1s ²		1s ¹	
$n_{\bar{p}}$					30		25		16		16	

4.2.1 Antiprotonic transitions

The incomplete suppression of the $\bar{p}\text{Kr}(16-15)$ and $\bar{p}\text{Kr}(15-14)$ lines shows again that the cascade does not proceed exclusively through circular states allowing already a partial depletion of the K shell before the antiproton reaches the level $n_{\bar{p}} = 16$ by $\Delta n > 1$ transitions. By the time the antiproton has reached $n_{\bar{p}} = 14$, however, the observed maximal line yield requires complete ionisation (Table 10).

Suppression of X-rays for transitions starting from $n_{\bar{p}} > 24$ in combination with saturated yields of the lines (23–22) to (17–16) suggests that L electron removal takes place the same way as for K electrons, however, with about two electrons already removed when reaching the L-emission threshold for $\Delta n_{\bar{p}} = 1$ transitions. Again, such a removal must be caused by $\Delta n_{\bar{p}} > 1$ de-excitation in the higher cascade. Otherwise, as the calculations of elec-

**Fig. 9.** Spectrum of antiprotonic argon in the region of electronic K X-rays.**Table 9.** Line assignment in the spectrum of antiprotonic argon (Fig. 2 and 9). The errors are statistical only.

experimental energy (eV)	relative intensity (%)	explanation	theoretical energy (keV)
2182 ± 11	91.6 ± 14.0	$\bar{p}\text{Ar}(20-19)1s^2$	2129
2516 ± 5	146.9 ± 11.1	$\bar{p}\text{Ar}(19-18)1s^2$	2495
2949 ± 3	166.2 ± 9.5	$\bar{p}\text{Ar}(18-17)/\text{Ar } K\alpha$	2952/2957
3494 ± 11	47.9 ± 3.2	$\bar{p}\text{Ar}(17-16)$	3523
3768 ± 10	36.3 ± 2.4	<i>not identified</i>	
4242 ± 5	27.1 ± 1.0	$\bar{p}\text{Ar}(16-15)$	4251
5197 ± 2	81.8 ± 2.2	$\bar{p}\text{Ar}(15-14)$	5196
6440 ± 1	88.1 ± 2.1	$\bar{p}\text{Ar}(14-13)$	6441
7219 ± 38	1.0 ± 0.3	$\bar{p}\text{O}(8-7)$	7206
8117 ± 1	91.7 ± 2.2	$\bar{p}\text{Ar}(13-12)$	8120
10443 ± 1	100	$\bar{p}\text{Ar}(12-11)$	10438
11104 ± 16	5.5 ± 0.3	$\bar{p}\text{O}(7-6)$	11110
13723 ± 2	97.7 ± 2.1	$\bar{p}\text{Ar}(11-10)$	13729
18560 ± 2	90.3 ± 1.9	$\bar{p}\text{Ar}(10-9)$	18566
22887 ± 24	5.0 ± 0.3	<i>not identified</i>	
25977 ± 3	86.6 ± 1.8	$\bar{p}\text{Ar}(9-8)$	25972

tronic binding and antiprotonic transition energies show, for a fully occupied L shell the removal of L electrons by Auger emission can start the earliest at $n_{\bar{p}} \approx 29$ for circular transitions and the lines (24–23), (23–22), and (22–21) would be still suppressed (Table 3). The $\bar{p}\text{Kr}(23-22)$ transition reaches almost the maximum yield, i.e., the last L electron is removed in the step (24–23).

Below 3.5 keV down to 1.6 keV indications of more antiprotonic transitions are seen (Fig. 11). Such lines can be

Table 7. Electron binding energies BE and effective nuclear charge Z_{eff}^e acting on the electrons of Xe. For explanation of symbols see Table 5.

levels	$BE(eV)$	Z_{eff}^e	$BE(eV)$	Z_{eff}^e	$BE(eV)$	Z_{eff}^e	$BE(eV)$	Z_{eff}^e	$BE(eV)$	Z_{eff}^e	$BE(eV)$	Z_{eff}^e
1s	34624	53.3	34740	53.3	35500	53.3	37647	53.3	40271	53.6	41300	54
					<i>34106</i>	<i>52.3</i>	<i>36197</i>	<i>52.3</i>	<i>38796</i>	<i>52.6</i>	<i>39785</i>	<i>53</i>
2s	5590	50.0	5608	50	6382	50.0	8303	50.9				
					<i>6042</i>	<i>49.0</i>	<i>7946</i>	<i>49.9</i>				
2p _{1/2}	5149	48.9	5259	49	5999	49.0	7998	49.8				
					<i>5701</i>	<i>47.5</i>	<i>7647</i>	<i>48.8</i>				
2p _{3/2}	4825	48.3	4937	48	5675	48.5	7661	49.5				
					<i>5403</i>	<i>47.5</i>	<i>7339</i>	<i>48.5</i>				
3s	1166	43.1	1280	43	1962	43.6						
					<i>1849</i>	<i>42.6</i>						
3p _{1/2}	1022	41.1	1134	41	1820	42						
					<i>1709</i>	<i>40.2</i>						
3p _{3/2}	960	40.3	1071	40	1754	41						
					<i>1650</i>							
3d _{3/2}	707	37.4	819	37	1511	38.4						
					<i>1413</i>	<i>37.4</i>						
3d _{5/2}	694	37.2	806	37	1497	38.3						
					<i>1401</i>	<i>37.2</i>						
4s	229	33.0	338	33								
4p _{1/2}	175	30.4	284	30.5								
4p _{3/2}	163	29.6	271	30								
4d _{3/2}	73.7	24.1	187	24								
4d _{5/2}	71.7	23.8	80	24								
5s	27.5	19.6										
5p _{1/2}	13.4	16.2										
5p _{3/2}	12.0	15.5										
no. of electrons	54		46		28		10		2		1	
configuration	1s ² 2s ² 2p ⁶ 3s ² 3p ⁶ 3d ¹⁰ 4s ² 4p ⁶ 4d ¹⁰ 5s ² 5p ⁶		1s ² 2s ² 2p ⁶ 3s ² 3p ⁶ 3d ¹⁰ 4s ² 4p ⁶ 4d ¹⁰		1s ² 2s ² 2p ⁶ 3s ² 3p ⁶ 3d ¹⁰		1s ² 2s ² 2p ⁶		1s ²		1s ¹	
$n_{\bar{p}}$					30		30		17		16	

tentatively assigned to radiative de-excitation after complete removal of all M and N electrons, but with the few L electrons present which are bound stronger than 3.5 keV. Interpreting the lines at 1.61 and 2.04 keV as the $\bar{p}\text{Kr}(34-33)$ and $\bar{p}\text{Kr}(32-31)$ transitions, the line yield can be as high as 40% and 70%, respectively. Needless to say, that a clear distinction between background and X-ray transition is difficult because of the nearby detection threshold and the non-resolution of other possible lines.

4.2.2 K-X-ray region

The complex structure visible in the range 12 to 14 keV (Fig. 10 – top) is mostly attributed to electronic X-ray emission during the antiprotonic cascade. For the discussion K transition energies of some electron shell configurations are plotted in the lower part of Fig. 10 as a function of the antiprotonic state $n_{\bar{p}}$. The decrease in energy of about 0.75 keV reflects the reduction of the effective charge seen by the electrons by one unit from krypton ($Z = 36$) to a bromine-like ($Z = 35$) nucleus when the antiproton penetrates below the rms radii of the K shell.

The most prominent satellite peak has an energy of 12.287 keV with a relative intensity of 24% of the $\bar{p}\text{Kr}(18-17)$ transition (Table 10). Considering first the case of the $1s^1 2p^1 \rightarrow 1s^2$ transition energy in the presence of a complete L shell, the energy can be reached only if the antiproton is still at or above the K shell, i. e., $n_{\bar{p}} \geq 40$, because of screening. K hole production at that level requires $\Delta n_{\bar{p}} \gg 1$ Auger transitions (Table 1) and is very unlikely in the presence of L electrons. For already significantly ionised krypton with only very few L electrons left, the $K\alpha$ transition energy corresponds to an antiproton state at $n_{\bar{p}} \approx 20$. Indeed from $n_{\bar{p}} \approx 20$ on, the $\Delta n_{\bar{p}} = 2$ Auger transition is able to ionise the K shell. As can be seen from Fig. 10, no other configuration is able to reach 12.29 keV. Furthermore, an indication of the $K\beta$ analogue is found at 15.09 keV.

The line found at an energy of 12.696 keV could be due to $K\alpha$ fluorescence by radiation excitation. However, an inclusion of the $K\beta$ line at 14.1 keV with a $K\alpha/K\beta$ intensity ratio of 5.8 [49] improves only slightly the fit of the low-energy side of the $\bar{p}\text{Kr}(17-16)$ transition. In addition, the energy is about 60 eV too high for normal krypton fluo-

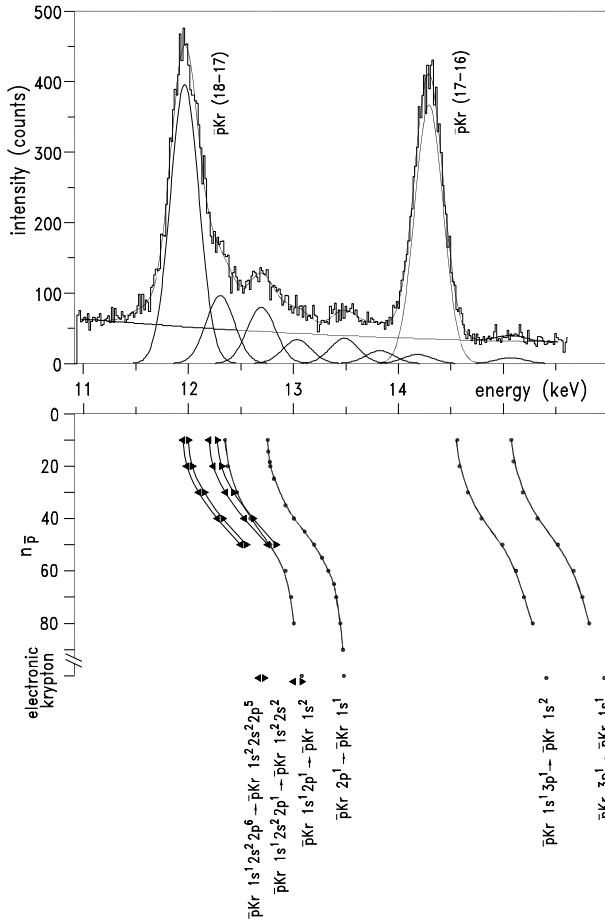


Fig. 10. Top – Spectrum antiprotonic krypton expanded in the energy range of the electronic K X-rays. Bottom – Calculated energies of electronic transitions as a function of the antiproton orbit. Double lines represent the $K\alpha_{1,2}$ doublet. Symbols close to the legend correspond to krypton atoms without an antiproton present.

rescence. As discussed earlier [23] a second Auger emission creating a double K hole before radiative de-excitation of one remaining L electron, again at $n_{\bar{p}} \approx 20$, leads to such a high electron transition energy. This requires a high degree of ionisation at that stage, which is not excluded because of the high yield of the $\bar{p}\text{Kr}(25-24)$ and subsequent lines. Because the transition occurs in an atom with a double K hole it is an analogue to the hypersatellite case.

If interpreted as a $\bar{p}\text{Kr}$ electronic transition, the line at 12.954 keV requires almost complete depletion at $n_{\bar{p}} \approx 40$. In addition, again the production of a double K hole is needed to allow a $2p \rightarrow 1s$ transition. Such a high degree of ionisation, however, is very unlikely at this stage of the antiprotonic cascade. So, no interpretation is given.

Capture from the continuum or $\Delta n_{\bar{p}} \gg 1$ steps from very high states to about $n_{\bar{p}} = 40$, where screening of one nuclear charge is not yet complete, produces only very low ionisation states. In the case of hardly depleted electron shells a K hole leads to K-X-ray emission in a bromine-like atom. An energy of 13.5 keV corresponds to $K\beta$ emission from such systems. The measured energy is

13.487 keV with a relative yield of 8%. The corresponding $K\alpha$ coincides exactly with the $\bar{p}\text{Kr}(18-17)$ transition (relative yield 100%). However, assuming $K\alpha/K\beta$ ratios comparable to normal atoms, the $K\alpha$ contribution should be visible as an outstanding high yield of the (18-17) line. This is not observed.

Close to the line at 13.487 keV is the antiprotonic transition $\bar{p}\text{Al}(9-8)$ having a calculated energy of 13.38 keV. Indeed at 19.5 and 30.1 keV more $\bar{p}\text{Al}$ transitions are observed. But for the line under discussion, first the energy is too high by 100 eV and secondly the measured yield is too high relative to the other $\bar{p}\text{Al}$ transitions.

Furthermore there is evidence for a line at 13.81 keV, the energy of which fits to the $\bar{p}\text{Kr}(22-20)$ transition (13.869 keV) in the presence of two K electrons. It is noteworthy that no evidence for any further $\Delta n_{\bar{p}} = 2$ transition was found. A possible $\bar{p}\text{Kr}(23-21)$ transition is hidden below $\bar{p}\text{Kr}(17-16)$ line.

A second region with additional low-intensity lines is observed between the $\bar{p}\text{Kr}(19-18)$ and $\bar{p}\text{Kr}(18-17)$ transitions (Fig. 2). The largest component amounts to $6.1 \pm 1.1\%$ at 10.641 ± 32 keV. The energy range fits to electronic X-rays from few-electrons systems having a nuclear charge Z in the range of 31–34. The production of such atoms with $Z = 35 - 31$ by antiproton-nucleon annihilation at the nuclear surface has been observed by detection of γ -rays after capture [50]. However, at the time of annihilation the Kr atom can be assumed to be completely ionised as are then the daughter nuclei and, therefore, electron refilling has to occur. At the low pressure of 20 mbar collision rates are as low as $\approx 10^6/s$. In addition, the cross section for radiative recombination is calculated to be negligible [51]. Hence, no emission of K and L atomic X-rays is expected and an assignment for the small contaminations in this energy range remains open.

4.2.3 L-X-ray region

Below 4 keV a broad structure is observed together with the indications for higher antiprotonic transitions (Fig. 11). The energy range fits to electronic L X-rays at various higher charge states (around 2 keV), which requires the

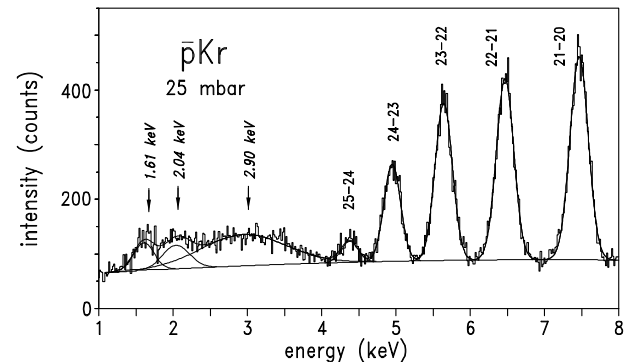


Fig. 11. Spectrum of antiprotonic krypton expanded in the energy range of the electronic L X-rays.

Table 10. Line assignment in the spectrum of antiprotonic krypton.

experimental energy (eV)	relative intensity (%)	explanation	theoretical energy (keV)
4369 ± 13	17.6 ± 2.4	$\bar{p}\text{Kr}(25-24)1s^2$	4341
4939 ± 3	64.2 ± 4.2	$\bar{p}\text{Kr}(24-23)1s^2$	4923
5627 ± 2	88.9 ± 2.8	$\bar{p}\text{Kr}(23-22)1s^2$	5613
6447 ± 2	87.1 ± 2.6	$\bar{p}\text{Kr}(22-21)1s^2$	6438
7445 ± 5	89.7 ± 3.8	$\bar{p}\text{Kr}(21-20)1s^2$	7431
8645 ± 2	85.0 ± 2.4	$\bar{p}\text{Kr}(20-19)1s^2$	8639
10133 ± 2	96.2 ± 2.6	$\bar{p}\text{Kr}(19-18)1s^2$	10123
10642 ± 32	6.1 ± 1.1	<i>not identified</i>	
11968 ± 7	100	$\bar{p}\text{Kr}(18-17)1s^2 + \text{''Br'' } K\alpha?$	11967
12287 ± 33	24.3 ± 1.5	$\bar{p}\text{Kr } n \approx 20 \ 1s2p \rightarrow 1s^2 \text{ el.}$	12290
12696 ± 24	20.4 ± 1.4	$\bar{p}\text{Kr } n \approx 20 \ 2p \rightarrow 1s \text{ el.}$	12760
		$K\alpha \text{ fluorescence?}$	12648/12597
12954 ± 32	8.6 ± 1.2	<i>not identified</i>	
13487 ± 20	9.0 ± 1.4	$\text{''Br'' } K\beta?$	
13814 ± 39	4.6 ± 1.0	$\bar{p}\text{Kr}(22-20) \text{ with } 1s^2 \text{ el.}$	13860
14288 ± 2	95.5 ± 2.3	$\bar{p}\text{Kr}(17-16)1s^2$	14286
15090 ± 43	2.4 ± 0.7	$\bar{p}\text{Kr } n \leq 14 \ 3p \rightarrow 1s \text{ el.}$	15080
17261 ± 12	11.6 ± 1.0	$\bar{p}\text{Kr}(16-15)$	17250
19537 ± 27	3.2 ± 0.8	$\bar{p}\text{Al}(8-7)$	19523
21090 ± 4	33.6 ± 1.2	$\bar{p}\text{Kr}(15-14)$	21084
26147 ± 3	89.4 ± 2.3	$\bar{p}\text{Kr}(14-13)$	26145
29052 ± 19	4.4 ± 0.6	<i>not identified</i>	
30146 ± 25	3.4 ± 0.5	$\bar{p}\text{Al}(7-6)$	30107
32962 ± 3	80.5 ± 2.2	$\bar{p}\text{Kr}(13-12)$	32965

presence of some M electrons. A rough estimate for the yield of the L-X-ray intensity is given to be 2 ± 1 per antiprotonic krypton atom.

4.3 Antiprotonic Xenon

In contrast to argon and krypton, the most prominent features of the antiprotonic xenon spectrum are two broad structures at 4.5 and 29 keV (Fig. 2). The energy range corresponds to electronic K and L X-rays of iodine to xenon. The large width of the distribution of about 3 and 2 keV, respectively, indicates that a large variety of ionisation states contributes. Antiprotonic transitions are observed as high as (29–28). The low-lying lines having energies above 60 keV exceed the detection range.

4.3.1 Antiprotonic transitions

Following the discussion of the antiprotonic cascade in Sec. 3.3 ionisation of the fully occupied M shell can commence at $n_{\bar{p}} \approx 68$ and ends with the $\bar{p}\text{Xe}(37-36)$ transition. Line yields around 20% for the transitions $\bar{p}\text{Xe}(29-28)$ to $\bar{p}\text{Xe}(24-23)$ constitutes evidence that indeed in some cases the M shell is depleted, when the antiproton reaches $n_{\bar{p}} = 29$ (Table 4). From $n_{\bar{p}} = 29$ on also L-shell depletion by $\Delta n_{\bar{p}} = 1$ transitions becomes possible.

We may note, that the occurrence of circular transitions from $n_{\bar{p}} = 29-27$ requires M-shell depletion, whereas the finite yield of the lines $\bar{p}\text{Xe}(26-25)$ to $\bar{p}\text{Xe}(17-16)$ is due to the increase of radiative de-excitation with increasing energy. Even more, the relative yields coincide rather accurately with the energy dependence of Γ_X/Γ_{tot} as expected from Ferrell's formula (Fig. 4). About two-thirds of the L electrons can be removed until the level $n_{\bar{p}} = 16$ is reached.

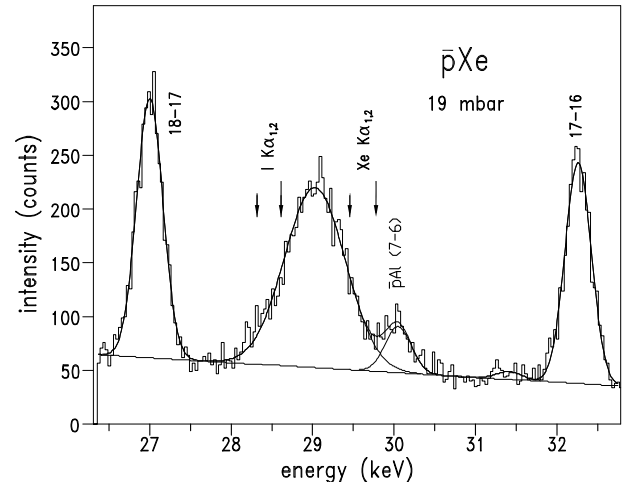
Even assuming atoms with a significant remaining N-shell electron population, the binding energies of the K electrons never become small enough to allow Auger emission at $n_{\bar{p}} = 17$ (Table 7). Therefore, the first de-excitation step being able to emit a K electron is the $\bar{p}\text{Xe}(16-15)$ transition. As then expected, the line yield drops to about the fraction suggested by Γ_X/Γ_{tot} . The observed non-saturation of the $\bar{p}\text{Xe}(14-13)$ yield is consistent with incomplete L-shell ionisation at $n_{\bar{p}} = 16$ as discussed above.

An approximately linear increase in intensity of the transitions with $n_{\bar{p}} \leq 15$, as suggested by Ferrell's formula is not observed. Because of the increasing electron depletion even higher X-ray yields are expected. No explanation was found for such a behaviour.

4.3.2 Electronic K and L X-rays

The broad structure between the transitions $\bar{p}\text{Xe}(18-17)$ and $\bar{p}\text{Xe}(17-16)$ originates from electronic X-rays from partially depleted xenon (Fig. 12). About two K X-rays are emitted per formed antiprotonic xenon (Table 11).

The lower limit coincides approximately with electronic states from iodine, which could originate from higher lying $\Delta n_{\bar{p}} \gg 1$ transitions and require an almost complete electron shell. Because of the dominance of $\Delta n_{\bar{p}} = 1$ and 2 Auger transitions, in particular with the outer shells present, the strong decrease of intensity towards lower energies seems to be natural. The upper limit is at about the

**Fig. 12.** Spectrum of antiprotonic xenon expanded in the energy range of electronic K X-rays. The arrows indicate the energies of the iodine and xenon $K\alpha$ doublets (see Table 8).

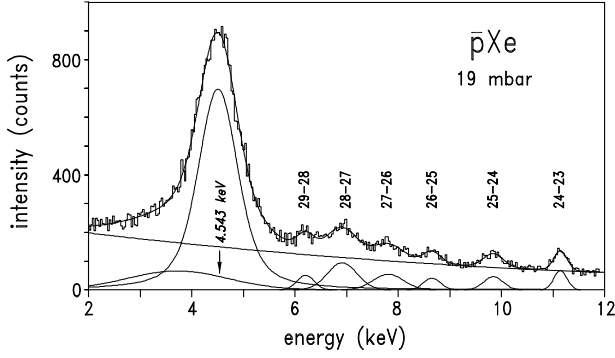


Fig. 13. Spectrum of antiprotonic xenon expanded in the energy range of electronic L X-rays.

energy of an electronic $K\alpha_1$ for highly ionised $\bar{p}\text{Xe}$ with significant L-shell ionisation (Table 7). The central energy of 29.1 keV corresponds to K hole refilling in the presence of a significantly populated M shell as can be seen from inspection of the columns with $n_{\bar{p}} = 30$ in Table 7. Higher and lower energies require a higher and lower degree of ionisation, respectively.

No extra intensity from normal xenon $K\alpha$ and $K\beta$ fluorescence could be identified. In Fig. 12, the arrows mark the positions of the iodine and xenon $K\alpha$ fluorescence lines.

Table 11. Line assignment in the spectrum of antiprotonic xenon.

experimental energy (eV)	relative intensity (%)	explanation	theoretical energy (keV)
4560 \pm 6	$\approx 1250 \pm 45$	L X-rays	
6262 \pm 19	29.9 \pm 3.8	$\bar{p}\text{Xe}(29-28)$	6219
6960 \pm 14	44.5 \pm 3.3	$\bar{p}\text{Xe}(28-27)$	6928
7771 \pm 15	22.4 \pm 2.4	$\bar{p}\text{Xe}(27-26)$	7750
8680 \pm 20	10.3 \pm 1.7	$\bar{p}\text{Xe}(26-25)$	8704
9877 \pm 19	16.8 \pm 1.6	$\bar{p}\text{Xe}(25-24)$	9822
11163 \pm 10	20.9 \pm 1.4	$\bar{p}\text{Xe}(24-23)$	11138
12717 \pm 7	30.2 \pm 1.7	$\bar{p}\text{Xe}(23-22)$	12698
14578 \pm 5	49.5 \pm 2.0	$\bar{p}\text{Xe}(22-21)$	14563
16825 \pm 4	62.7 \pm 2.1	$\bar{p}\text{Xe}(21-20)$	16810
19564 \pm 4	78.0 \pm 2.5	$\bar{p}\text{Xe}(20-19)$	19543
22912 \pm 4	86.3 \pm 2.6	$\bar{p}\text{Xe}(19-18)$	22901
23823 \pm 24	9.7 \pm 1.1	$\bar{p}\text{Xe}(24-22)$	23826
25828 \pm 25	10.6 \pm 1.3	<i>not identified</i>	
27095 \pm 4	100	$\bar{p}\text{Xe}(18-17)$	27073
29118 \pm 8	228.7 \pm 7.3	K X-rays	
30141 \pm 23	11.6 \pm 1.6	$\bar{p}\text{Al}(7-6)$	30107
31503 \pm 65	3.1 \pm 1.1	<i>not identified</i>	
32336 \pm 4	91.3 \pm 3.0	$\bar{p}\text{Xe}(17-16)$	32321
39040 \pm 11	38.7 \pm 2.2	$\bar{p}\text{Xe}(16-15)$	39028
42212 \pm 55	6.3 \pm 1.8	<i>not identified</i>	
47714 \pm 11	46.5 \pm 2.6	$\bar{p}\text{Xe}(15-14)$	47708
50036 \pm 61	6.7 \pm 1.8	$\bar{p}\text{Al}(6-5)$	49989
59152 \pm 17	45.8 \pm 3.3	$\bar{p}\text{Xe}(14-13)$	59167

About 10 L X-rays are emitted per $\bar{p}\text{Xe}$ atom, i. e., at least 10 times L-electron emission and subsequent refilling (Fig. 13). It requires both the presence of M electrons and a rather complete depletion of the N shell, because otherwise the L vacancies are filled mainly by radiationless processes [24]. The maximum of the distribution at about 4.5 keV corresponds to L-X-ray energies for depleted N and O shells with commencing M electron emission. The absence of $\bar{p}\text{Xe}$ lines below 3.5 keV shows that the M shell does not deplete before $n_{\bar{p}} \approx 29$.

5 Summary

The characteristic X-radiation from the antiprotonic noble gases argon, krypton, and xenon has been studied in order to elucidate the role of the non-radiative de-excitation mechanism on the X-ray yields of the antiprotonic lines. A number of additional lines in the X-ray spectra of the noble gases have been tentatively assigned to electronic transitions caused by electron de-excitation after Auger emission during the antiprotonic cascade. A few lines remain unexplained so far or are not unambiguously assigned.

In general, the high degree of circularity of the antiprotonic cascade is evident from the specific depletion sequence showing up in the spectrum as alternating low and high yield antiprotonic X-ray transitions. As concluded earlier [22] complete ionisation is reached for krypton, which is not the case for xenon. Therefore, the $\bar{p}\text{Xe}$ spectrum is much richer in electronic L and K X-rays than that of $\bar{p}\text{Ar}$ or $\bar{p}\text{Kr}$.

Electronic X-rays are concentrated in the energy ranges corresponding to about the emission bands of the principal shells. The complexity of states cannot be resolved with semiconductor detectors. The details of such structures may be resolved in future by high-resolution devices like crystal spectrometers having at least two orders of magnitude higher resolving power. Also Auger electron spectroscopy might be resumed being a powerful technique to explore the initial stages of the de-excitation cascade especially if, e. g., lowest-density targets like gas jets can be used.

Such studies will become feasible at antiproton facilities like the one planned at the research center GSI [52]. There, sufficiently intense low-energy antiproton beams suited for high-statistics antiproton stop experiments could be provided.

Acknowledgements

Khalid Rashid wishes to express his gratitude to the Forschungszentrum Jülich and the University of Kassel for hosting the visits. KR also acknowledges with thanks the grant from Alexander-von-Humboldt foundation, Germany, and from the Higher Education Commission, Pakistan. The authors are grateful to K.-P. Wieder of the Forschungszentrum Jülich for the numerous drawings and Josef Anton of the University of Kassel for much technical support.

Laboratoire Kastler Brossel is Unité Mixte de Recherche du CNRS, de l'École Normale Supérieure et de l'Université Pierre et Marie Curie n° C8552.

References

1. P.K. Haff and T.A. Tombrello, *Annals of Physics*, **86**, 178 (1974)
2. P. Vogel, P.K. Haff, V. Akylas, and A. Winther, *Nucl. Phys. A* **254**, 445 (1975)
3. P. Vogel, A. Winther, and V. Akylas, *Phys. Lett. B* **70**, 39 (1977)
4. H. Schneuwly, V.I. Pokrovsky, and V.I. Ponomarev, *Nucl. Phys. A* **3122**, 419 (1978)
5. H. Daniel, *Z. Phys. A* **291**, 29 (1979)
6. T. von Egidy, D.H. Jakubassa-Amundsen, and F.J. Hartmann, *Phys. Rev. A* **29**, 445 (1984)
7. F.J. Hartmann, in *Proceedings of Physics of Exotic Atoms on Electromagnetic Cascade and Chemistry*, 1989, Erice, Italy, 1989 (Plenum Press, New York, 1990) p. 23 and p. 127, and references therein
8. J.S. Cohen, *Rep. Prog. Phys.* **67**, 1769 (2004)
9. G. Zschornack, *Sov. J. Part. Nucl.* **14**(4), 349 (1983)
10. K. Kaeser, T. Dubler, B. Robert-Tissot, L.A. Schaller, L. Schellenberg, and H. Schneuwly, *Helv. Phys. Acta* **52**, 238 (1979)
11. F.J. Hartmann, R. Bergmann, H. Daniel, H.-J. Pfeiffer, T. von Egidy, and W. Wilhelm, *Z. Phys. A* **305**, 189 (1982)
12. V.R. Akylas and P. Vogel, *Comp. Phys. Comm.* **15**, 291 (1978)
13. E. Fermi and E. Teller, *Phys. Rev.* **72**, 399 (1947)
14. K. Kirch, D. Abbot, B. Bach, P. Hauser, P. Indelicato, F. Kottmann, J. Missimer, P. Patte, R.T. Siegel, L.M. Simons, and D. Viel, *Phys. Rev. A* **59**, 3375 (1999)
15. D. Horváth and R.M. Lambrecht, *Exotic Atoms* (North-Holland, Amsterdam, 1984)
16. A. Shinohara, T. Muroyama, J. Shintai, J. Kurachi, M. Furukawa, T. Miura, Y. Yoshimura, T. Saito, T. Ohdaira, and N. Imanishi, *Phys. Rev. A* **53**, 130 (1996)
17. J.S. Cohen, *Phys. Rev. A* **62**, 022512 (2000)
18. G.R. Burbidge and A.H. de Borde, *Phys. Rev.* **89**, 189 (1953)
19. A.H. de Borde, *Proc. Phys. Soc. (London)* **A67**, 57 (1954)
20. G.T. Condo, R.D. Hill, and A.D. Martin, *Phys. Rev.* **133**, A1280 (1964)
21. R. Callies, H. Daniel, F.J. Hartmann, and W. Neumann, *Phys. Lett.* **91A**, 441 (1982)
22. R. Bacher, P. Blüm, D. Gotta, K. Heitlinger, M. Schneider, J. Missimer, L.M. Simons and K. Elsener, *Phys. Rev. A* **38**, 4395 (1988)
23. L.M. Simons, D. Abbot, B. Bach, R. Bacher, A. Badertscher, P. Blüm, P. DeCecco, J. Eades, J. Egger, K. Elsener, D. Gotta, P. Hauser, K. Heitlinger, D. Horvath, F. Kottmann, E. Morenzoni, J. Missimer, J. J. Reidy, R. Siegel, D. Taquu and D. Viel, *Nucl. Inst. Meth. B* **87**, 293 (1994)
24. O. Keski-Rahkonen and R.A. Krause, *At. Data and Nucl. Data Tables* **14**, 139 (1974)
25. M.O. Krause and Th.A. Carlson, *Phys. Rev.* **158**, 158 (1967)
26. R. Arlt, Z. Ganzorik, T. Krogulski, H.-G. Ortlepp, S.M. Polikanov, B.M. Sabirov, V.D. Fromm, U. Schmidt, G. Schnefli, and R. Engfer, *JETP Letters*, vol. **20**, no. 9, 291 (1974)
27. W.D. Fromm, Dz. Gansorig, T. Krogulski, H.-G. Ortlepp, S.M. Polikanov, B.M. Sabirov, U. Schmidt, R. Arlt, R. Engfer, and H. Schneuwly, *Phys. Lett.* **55B**, 377 (1975)
28. H. Schneuwly and P. Vogel, *Phys. Rev. A* **22**, 2801 (1980)
29. K. Ninomiya, H. Sugiura, Y. Kasamatsu, H. Kikunaga, N. Kinoshita, Y. Tani, H. Hasegawa, M. Yatsukawa, K. Takamiya, W. Sato, H. Matsumura, A. Yokoyama, K. Sueki, Y. Hamajima, T. Miura, A. Shinohara, *Radiocim. Acta* **93**, 515 (2005)
30. R. Bacher, D. Gotta, L.M. Simons, J. Missimer, and N.C. Mukhopadhyay, *Phys. Rev. Lett.* **54**, 2087 (1985)
31. P. Hauser, K. Kirch, F. Kottmann, L.M. Simons, *Nucl. Instr. Meth. A* **411**, 389 (1998)
32. R. Bacher, Ph.D. thesis, University of Karlsruhe and Kernforschungszentrum Karlsruhe, 1987, report no. 4347, ISSN 0303-4003
33. J.P. Desclaux, *A Relativistic Multiconfiguration Dirac-Fock Package*, in *Methods and Techniques in Computational Chemistry*, edited by E. Clementi, (STEF, Cagliari, 1993), vol. A: Small Systems of METTEC, p. 253
34. H. Poth, *Compilation of Data from Hadronic Atoms* (Fachinform. Zentr. Karlsruhe, Germany, 1979), Physics Data, No.14-1 (1979), ISSN 0344-8401, 1979
35. LEAR experiment PS175, PSCC/80-99/PSCC/P 27 (1980)
36. R. Bacher, P. Blüm, D. Gotta, K. Heitlinger, D. Rohmann, M. Schneider, J. Egger, L. M. Simons, and K. Elsener, *Z. Phys. A* **334**, 93 (1989)
37. M. Schneider, R. Bacher, P. Blüm, D. Gotta, K. Heitlinger, W. Kunold, D. Rohmann, J. Egger, L.M. Simons, and K. Elsener, *Z. Phys. A* **338**, 217 (1991)
38. K. Heitlinger, R. Bacher, A. Badertscher, P. Blüm, J. Eades, J. Egger, K. Elsener, D. Gotta, E. Morenzoni, and L.M. Simons, *Z. Phys. A* **342**, 359 (1992)
39. W.M.J. Veigele, *At. Data and Nucl. Data Tables* **5**, 51 (1973)
40. R.A. Ferrell, *Phys. Rev. Lett.* **4**, 425 (1960)
41. G.T. Condo, *Phys. Lett.* **9**, 65 (1964)
42. J.E. Russell, *Phys. Rev. A* **1**, 742 (1970)
43. T. Yamazaki, N. Morita, R.S. Hayano, E. Widmann, J. Eades, *Phys. Rep.* **366**, 183 (2002)
44. P. Vogel, *Phys. Rev. A* **7**, 63 (1973)
45. B. Fricke, *Z. Naturforsch.* **30a**, 1328 (1975)
46. P. Vogel, A. Zehnder, A.L. Carter, M.S. Dixit, E.P. Hincks, D. Kessler, J.S. Wadden, C.K. Hargrove, R.J. McKee, H. Mes, and H.L. Anderson, *Phys. Rev. A* **15**, 76 (1977)
47. J.M. Hansteen, O.M. Johnson, and L. Kocbach, *At. Data and Nucl. Data Tables* **15**, 305 (1975)
48. R. Deslattes, E.G. Kessler, Jr., P. Indelicato, L. de Billy, E. Lindroth, and J. Anton, *Rev. Mod. Phys.*, vol. **75**, no. 1, 35 (2003)
49. S.I. Salem, S.L. Panossian, and M.O. Krause, *At. Data and Nucl. Data Tables* **14**, 91 (1974)
50. E.F. Moser, H. Daniel, T. von Egidy, F.J. Hartmann, W. Kanert, G. Schmidt, M. Nicholas, and J.J. Reidy, *Phys. Lett. B* **179**, 25 (1986)
51. G.A. Baker, Jr., *Phys. Rev.* **117**, 1130 (1960)
52. FLAIR project, <http://www.gsi.de/fair/experiments/flair>